The Astrophysical Journal, 692:1294–1304, 2009 February 20 doi:10.1088/0004-637X/692/2/1294

Fe xiii DENSITY DIAGNOSTICS IN THE EIS OBSERVING WAVELENGTHS

T. Watanabe[1,2], H. Hara[1,2], N. Yamamoto[3], D. Kato[4], H. A. Sakaue[4], I. Murakami[4], T. Kato[4], N. Nakamura[5], and P. R. Young[6]

[1] National Astronomical Observatory, Mitaka, Tokyo 181-8588, Japan; watanabe@uvlab.mtk.nao.ac.jp
[2] Graduate University for Advanced Studies, Hayama, Miura-gun, Kanagawa Pref. 240-0193, Japan
[3] Osaka University, Suita, Osaka 565-0871, Japan
[4] National Institute for Fusion Science, Toki, Gifu Pref. 509-5292, Japan
[5] University of Electro-Communications, Chofu, Tokyo 182-8585, Japan
[6] Rutherford Appleton Laboratory, Chilton, Didcot OX11 0QX, UK
Received 2008 June 18; accepted 2008 October 27; published 2009 February 24

ABSTRACT

The diagnostic capability of Fe xiii line features seen in the 170–210 Å waveband of the EUV Imaging Spectrometer (EIS) on *Hinode* is investigated, with emphasis on density diagnostics applied to solar active regions. Four diagnostic line pairs are found to yield consistent densities ranging from $10^{8.5}$ to $10^{9.5}$ cm^{-3} across an active region using a new theoretical model of the ion. In separate EIS observations of a small flare, the widely used line pair, Fe xiii λ203.8/λ202.0, is found to reach the high density limit predicted by a new theoretical model of the iron ion.

Key words: atomic processes – line: formation – Sun: corona – Sun: flares – Sun: UV radiation

1. INTRODUCTION

The EUV Imaging Spectrometer (EIS) on board the *Hinode* satellite observes solar emission lines at EUV wavelengths with high spatial and spectral resolution (Culhane et al. 2007). The two wavelength bands observed with EIS are 170–210 Å and 250–290 Å, and include emission lines of He ii and a wide range of iron ions from Fe viii to Fe xxiv, formed in the temperature range $4.7 \leqslant \log T_e \leqslant 7.2$. The quality of the EIS spectra is excellent and the EIS instrument reveals a large number of emission lines throughout the two wavelength bands that offer exciting diagnostic opportunities (Young et al. 2007; Brown et al. 2008). The wide range of iron ions in particular means that derived emission measure distributions as a function of temperature are free from abundance uncertainties (Watanabe et al. 2007).

Among the emission lines of the various iron species, the Fe xiii lines found in the EIS short wavelength band (170–210 Å) are particularly important as they provide several line pairs sensitive to the density of the coronal plasma. As an independent parameter to the emission measure, the density is crucial to determining the plasma filling factor, i.e., the fraction of the observed plasma volume that is emitting radiation. Landi (2002) analyzed measurements of the EUV Fe xiii lines from the SERTS rocket experiments (Brosius et al. 1996, 1998, 2000), and compared with two different atomic models of the ion that used different electron collision data sets: the close-coupling calculations of Gupta & Tayal (1998) and the distorted-wave calculations of Fawcett & Mason (1989). Electron densities estimated by various line ratios differ by ~ 2 between the theoretical calculations, and a definitive conclusion could not be reached on which of the two theoretical data sets is to be preferred, although the analysis of the SERTS-95 ratios between $3s^23p3d$ and $3s3p^3$ lines has shown that in a few cases the close-coupling data set gives a better agreement with the observations than the distorted-wave one. Keenan et al. (2007) compared the same SERTS observations with a new model that incorporated the *R*-matrix calculations of Aggarwal & Keenan (2005), and concluded that the best line pair density diagnostics in the wavelength range 170–225 Å are λ200.03/λ202.04 and λ203.17/λ202.04, while problems were identified with the λ204.26/λ200.03 and λ209.63/λ204.26 ratios. Young et al. (2007) recommended the three Fe xiii lines λλ196.54, 202.04, and λ203.82 for density diagnostics in the EIS wavelength ranges based on an early study of the EIS data. Although the λ203.82 line (actually a self-blend of two Fe xiii lines at 203.79 and 203.83) is close to a Fe xii component at λ203.72, the high spectral resolution of EIS allows the lines to be resolved.

In this paper, Fe xiii lines observed by the EIS instrument are compared with predictions from the recent atomic model of Yamamoto et al. (2008) which incorporates the electron collision data of Aggarwal & Keenan (2005), and a revision of the CHIANTI v5.2 atomic model (Dere et al. 1997; Landi et al. 2006) that includes the electron collision data of Gupta & Tayal (1998). Electron number densities, n_e, are derived in the range $10^{8.5} \leqslant n_e \leqslant \sim 10^{11}$ cm^{-3}.

2. OBSERVATIONS

The EIS first light data sets presented by Watanabe et al. (2007) are analyzed here. At 23:40:44 UT on 2006 November 4 EIS was pointed at the bright core of solar active region 10921 (hereafter AR10921), and six exposures of duration 10, 20, 40, 80, 160, and 600 s were obtained at a fixed pointing with the 1″ slit. The same exposure sequence was then repeated with the 40″ slit. Full CCD spectra were obtained for all exposures. In this paper, the narrow slit spectra obtained with the 40 s exposure time (Figure 1) are analyzed as the strongest Fe xiii lines around λλ200–205 are not saturated with this exposure time.

For an example data set that exhibits a higher density, an observation of a C-class (C4.2) flare obtained on 2007 January 16 was chosen. EIS was in raster scanning mode, covering an area of 240″ × 240″ with the 1″ slit, and using a JPEG data-compression scheme (quality factor 95%) accommodated on the *Hinode* Mission Data Processor (MDP; Matsuzaki et al. 2007). The quality factor of 95% in the JPEG compression scheme is chosen to minimize the spectroscopic errors introduced by this lossy compression (H. Hara 2008, private communication). A total of 17 wavelength windows centered on individual emission lines was selected, including Fe xiii λ202.0 and λ203.8, and the

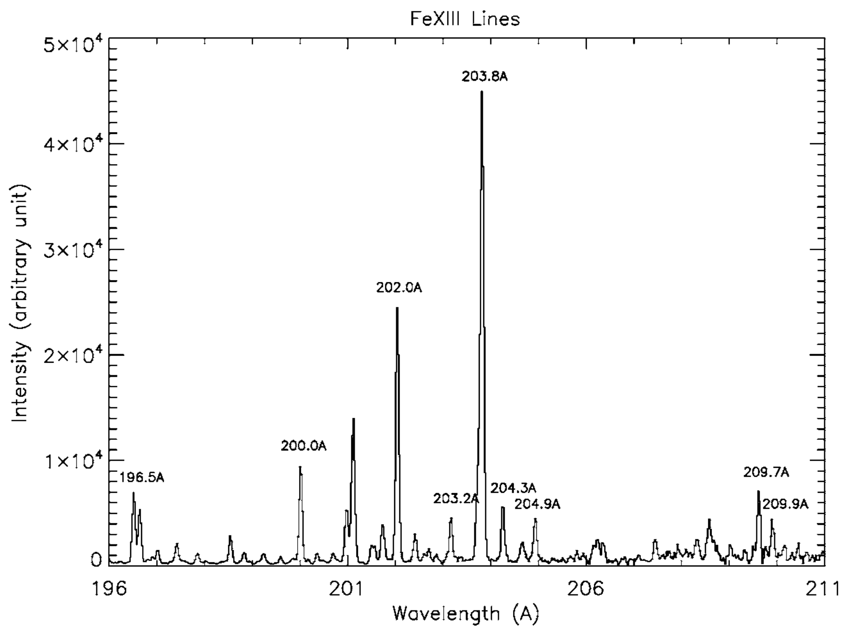

Figure 1. Active region spectrum in the wavelengths of 196–211 Å: strong Fe XIII emission lines are indicated.

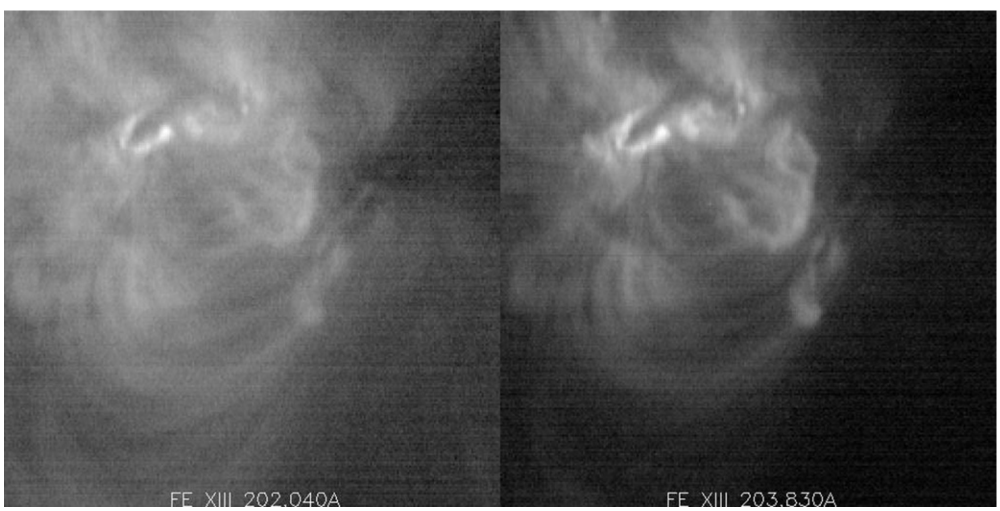

Figure 2. Fe XIII λ202.0 and λ203.8 images during a C-class flare of 2007 January 16 occurring in AR10938. The field of view of both images is 240″ × 240″.

exposure time was 5 s. The EIS raster began at 02:20:30 UT and finished at 02:46:41 UT, with the flare taking place at 02:22 UT as seen in *GOES* soft X-rays. Monochromatic images of Fe XIII λ202.0 and λ203.8 are shown in Figure 2.

In the full CCD spectra from AR10921, the unblended Fe XIII features listed in Table 1 were selected based on the analysis of Keenan et al. (2007) and Landi (2002), and their identifications are confirmed in the EIS line list of Brown et al. (2008). Thanks to the high spectral resolution of EIS, potential blending Fe XII line features near the Fe XIII lines at λ196.5 and λ203.8 can be resolved. Note that Fe XIII lines at λ201.1 and λ208.7 are excluded from the present analysis, as they are blended with Fe XII and Ca XV lines (Keenan et al. 2007).

Fe XIII lines appearing in the EIS short wavelength channel all originate from $3s^2 3p^2$–$3s^2 3p3d$ transitions. For the comparison of observations with theory, Keenan et al. (2007) noted three types of emission line intensity ratios, namely: (1) those which are predicted to be constant; (2) those which are predicted to be weakly sensitive to T_e and n_e; and (3) those which are predicted to be strongly n_e sensitive. In Table 1, the line pairs of λ200.0 versus λ203.8 and λ202.0 versus λ209.9 share the same upper levels, and thus correspond to the line pairs of category (1), while the line ratios of λ203.2/λ200.0, λ204.3/λ200.0, λ204.9/λ200.0, and λ209.6/λ204.3 belong to the category (2). Except for the category (1) ratio λ202.0/λ209.9, all ratios formed with λ202.0 are strongly density sensitive and belong to category (3) (see Figure 3).

In the flare data from 2007 January 16, only the Fe XIII λ202.0 and λ203.8 lines, forming a category (3) ratio, are observed.

3. DATA ANALYSIS

Two atomic models of Fe XIII are applied to the observational data. The first is a modified version of the model from v5.2 of the CHIANTI database (Dere et al. 1997; Landi et al. 2006). As noted by Young et al. (2009), the Fe XIII electron collision file in CHIANTI was inadvertently not updated to that of Gupta & Tayal (1998) in v3 of CHIANTI as stated in Dere et al. (2001), but in fact remained as the Fawcett & Mason (1989) data set from v1 of CHIANTI (Dere et al. 1997). In the present work,

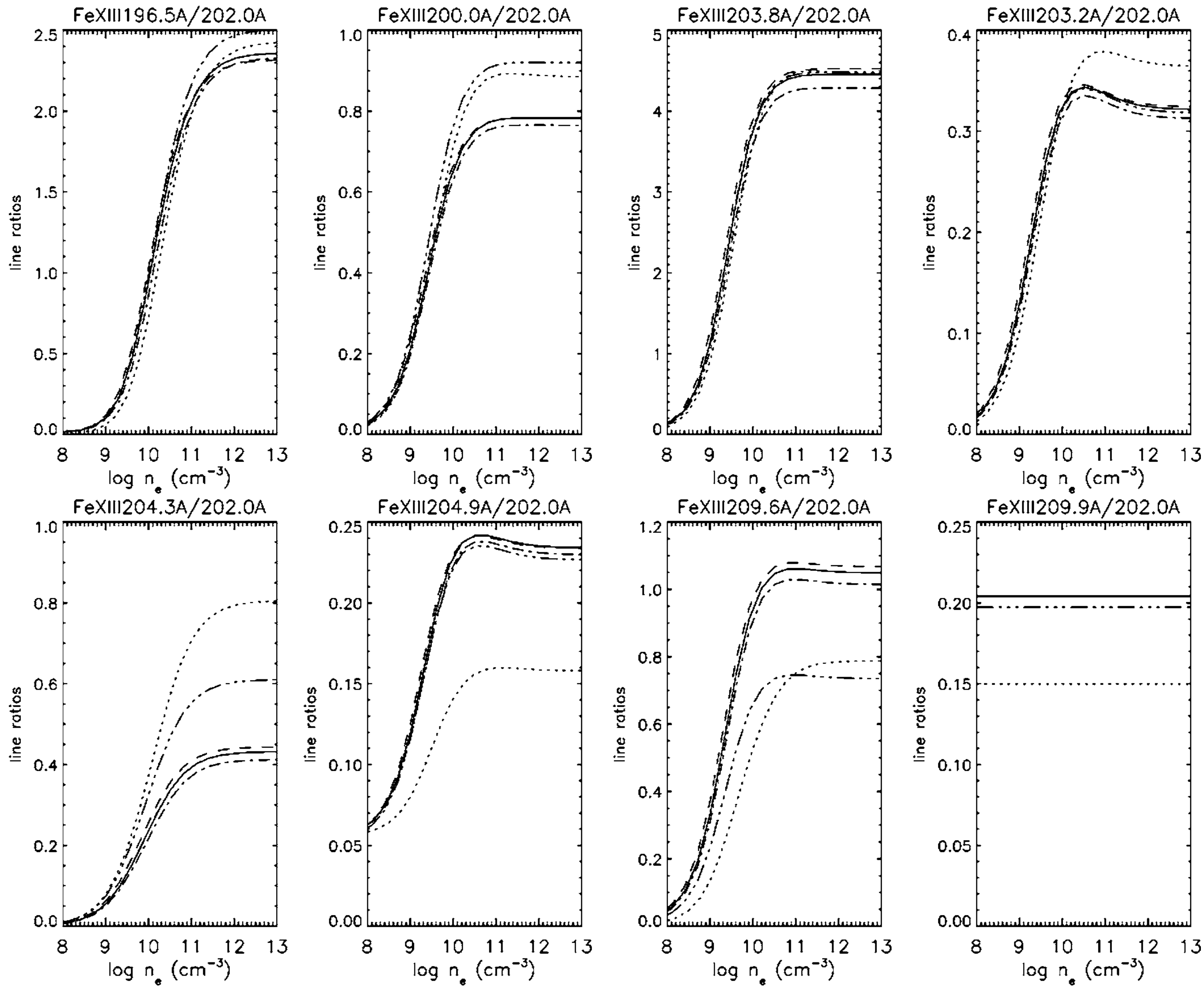

Figure 3. Fe XIII line intensity ratios against Fe XIII λ202.0 Å. Solid lines, dashed lines, and dot-dashed lines are from the predictions for log $T_e = 6.0$, 6.2, and 6.4 from the model of Y08, using the Aggarwal & Keenan (2005) data, while dotted lines are obtained by the revised CHIANTI code (v5.2) based on the Gupta & Tayal (1998) data set (CHIANTI-GT). Line ratios from the Y08 model configuration with radiative transition probabilities calculated by GRASP13 (Y08+GRASP13) are shown by dash-three-dots lines. See the text.

Table 1
Fe XIII lines appearing in EIS SW (Shorter Wavelengths)

Line Feature	Wavelength (Å)[a]	Configuration	CHIANTI[b] (s^{-1})	GRASP6[c] (s^{-1})	GRASP13[d] (s^{-1})	NIST[e] (s^{-1})
λ196.5	196.52	$3s^23p^2\ ^1D_2$–$3s^23p3d\ ^1F^o_3$	6.862+10[f]	8.275+10	7.3908+10	6.80+10
λ200.0	200.02	$3s^23p^2\ ^3P_1$–$3s^23p3d\ ^3D^o_2$	2.368+10	2.761+10	2.9279+10	
λ202.0	202.04	$3s^23p^2\ ^3P_0$–$3s^23p3d\ ^3P^o_1$	4.643+10	5.100+10	4.5491+10	
λ203.2	203.17	$3s^23p^2\ ^3P_1$–$3s^23p3d\ ^3P^o_0$	4.712+10	5.586+10	1.6005+10	
λ203.8	203.83	$3s^23p^2\ ^3P_2$–$3s^23p3d\ ^3D^o_3$	6.475+10	7.948+10	6.9486+10	6.50+10
	203.79	$3s^23p^2\ ^3P_2$–$3s^23p3d\ ^3D^o_2$	3.361+10	3.566+10	3.5499+10	
λ204.3	204.26	$3s^23p^2\ ^3P_1$–$3s^23p3d\ ^1D^o_2$	2.015+10	1.540+09	4.9464+10	
λ204.9	204.94	$3s^23p^2\ ^3P_2$–$3s^23p3d\ ^3D^o_1$	1.276+10	1.392+10	1.1984+10	
λ209.7	209.62	$3s^23p^2\ ^3P_1$–$3s^23p3d\ ^3P^o_2$	1.852+10	3.252+10	2.1115+10	
λ209.9	209.92	$3s^23p^2\ ^3P_2$–$3s^23p3d\ ^3P^o_1$	7.227+09	1.079+10	9.3164+09	

Notes.
[a] EIS observed wavelengths from Brown et al. (2008).
[b] CHIANTI v5.2 and CHIANTI-GT models.
[c] GRASP6 calculation by Aggarwal & Keenan (2005) used in the Y08 model (Yamamoto et al. 2008).
[d] GRASP13 calculation used in the K07 model (Keenan et al. 2007).
[e] NIST database: http://physics.nist.gov/PhysRefData/ASD/index.html.
[f] $a \pm b \equiv a \times 10^{\pm b}$.

the Gupta & Tayal (1998) data set has been swapped for the Fawcett & Mason (1989) data set and we refer to this model as the CHIANTI-GT model. Apart from the electron collision data, all other data remain the same as in the CHIANTI v5.2 model of the ion: energy levels are from Penn & Kuhn (1994), Jupen et al. (1993), and version 1.0 of the NIST Atomic Database; radiative decay rates are from Young (2004); and proton excitation rates are from Landman (1975). The CHIANTI-GT and CHIANTI v5.2 models consist of the 27 lowest fine structure levels. Electron impact excitation and radiative transitions are included only between the ground state and other levels. A few other transitions for radiative decay rates are also included.

The second Fe XIII model is that described in Yamamoto et al. (2008), which consists of 917 levels, including most of fine structure levels up to the principal quantum number $n = 5$. We refer to this model as the Y08 model and it accommodates the processes of excitation and de-excitation by electron impact, radiative decay, radiative recombination, ionization, three-body recombination, and autoionization, as well as dielectronic capture and dielectronic recombination. Transition probabilities and cross sections of these processes were calculated with the HULLAC code (Bar-Shalom et al. 2001). The effective collision strengths calculated with R-matrix code by Aggarwal & Keenan (2005), which are evaluated by Skobelev et al. (2007) and fitted by analytical functions, were used to calculate the electron impact excitation rate coefficients for transitions between $3s^23p^2$, $3s3p^3$, and $3s^23p3d$ states. The radiative transition probabilities calculated by the GRASP code (GRASP6) by Aggarwal & Keenan (2005) are used for the same transitions. The same Y08 model configuration replaced with radiative transition probabilities generated by the new code, GRASP13 (Keenan et al. 2007), is also calculated to see the effects of data replacement. The excitation rate coefficients for proton impact evaluated by Skobelev et al. (2006) are also included for the transitions between fine structure levels of the ground-state configuration, where the original data are from Landman (1975).

The difference of radiative transition probabilities between the CHIANTI-GT model and the Y08 model in which GRAPS6 calculation data by Aggarwal & Keenan (2005) were used for the same transitions as in the CHIANTI-GT model are mostly within a factor of about 2 for rates larger than 10^7 s.$^{-1}$ There are several transitions for which transition probabilities between two models differ by more than one order of magnitude, but these are not the lines in Table 1. The population densities are obtained by solving the coupled rate equations for each energy level. The calculation of the population density includes both ionization and recombination components in the model.

We note that the two models described above differ from those studied by Keenan et al. (2007). These authors used the CHIANTI v5.2 model which included the Fawcett & Mason (1989) electron collision data file rather than the Gupta & Tayal (1998) data file (see discussion above)—we refer to this as the CHIANTI-5 model. The second model used by Keenan et al. (2007) consisted of 97 levels and included electron collision data from Aggarwal & Keenan (2005), radiative data from the GRASP13 calculation of Aggarwal & Keenan (2004), experimental energy values from the NIST database, supplemented with theoretical energy values from Aggarwal & Keenan (2004), and proton excitation rates from Faucher & Landman (1977). We refer to the latter model as the K07 model.

Theoretical intensity ratios of the lines listed in Table 1 are plotted against density in Figure 3, in which the denominator line is fixed to Fe XIII λ202.0. For the Y08 model line ratios for temperatures log $T_e = 6.0$, 6.2, and 6.4 are calculated, and they show some temperature dependence. The ratios from the CHIANTI-GT model show much less temperature dependence and so only values calculated at log $T_e = 6.2$ are plotted. The iron M-shell ion line intensities depend on the population of metastable states, which are fine structure levels within the ground configuration. In Figure 3, theoretical line ratios calculated by the Y08 model with GRASP13 radiative rates (Y08+GRASP13) are also shown by dash-three-dots lines. Generally, the line ratios obtained with Y08+GRASP13 fall in between those calculated by CHIANTI-GT and Y08 (with GRASP6). Line ratios among strong lines in the upper panels of Figure 3 show no significant changes, while those from a few weaker line pairs are affected by the up-version GRASP calculation.

The line ratio of λ209.9/λ202.0 (bottom right panel of Figure 3) is independent of density, as the upper level of both lines is common, but the two models predict somewhat different values for this particular line intensity ratio. We note that the K07 model gives a value of 0.204 for this ratio, close to the Y08 model value. In Table 1 we compare the transition probabilities of the lines in the different models, i.e. the CHIANTI-GT model, the Y08 model with the GRASP6 calculation by Aggarwal & Keenan (2005), and the K07 model with the GRASP13 calculation. The difference in prediction of the line ratio λ209.9/λ202.0 mainly emerges from the difference in the transition probability between these two models, i.e. 0.156 for the CHIANTI-GT model and 0.212 for the Y08 model.

For the two Fe XIII ratios highlighted by Young et al. (2007), λ203.8/λ202.0 and λ196.5/λ202.0, significant differences are found for the four models discussed above and these are presented in Figure 4. Note that the two Fe XIII lines at λ203.79 and λ203.83 have been added to form the emissivity for λ203.8. For λ203.8/λ202.0 it can be seen that the Y08 and CHIANTI-GT models are in very good agreement. However, the CHIANTI-5 model prediction is significantly below these two models, while the HULLAC model is higher. For λ196.5/λ202.0 the Y08 and CHIANTI-GT models are in good agreement, as is HULLAC, but the CHIANTI-5 model ratio again has lower values than the others.

For other ratios we note that significant differences can be seen between the CHIANTI-GT and Y08 models in predictions of the high density limits for the λ200.0/λ202.0 and λ203.2/λ202.0 ratios recommended by Keenan et al. (2007), as well as the ratios of λλ204.3, 204.9, and 209.6 relative to λ202.0. For the λ196.5/λ202.0 and λ203.8/λ202.0 ratios recommended by Young et al. (2007), however, the predictions are in good agreement at all densities.

In order to extract the total line intensities for each spectral line, multiple Gaussian fits were performed to the spectral regions centered around each Fe XIII emission line feature listed in Table 1. Known features and contributions of the other ion species are taken into account, and example Gaussian fits to the various Fe XIII lines are presented in Figure 5. The fitting is performed in the central part (100″ interval; pixel positions along the slit: 200–300) of AR10921.

4. ACTIVE REGION DATA SET

Following the fits to the Fe XIII emission lines along the EIS slit, intensity ratios can be formed for the density sensitive line pairs and these are displayed in Figure 6. The accuracy of fitting

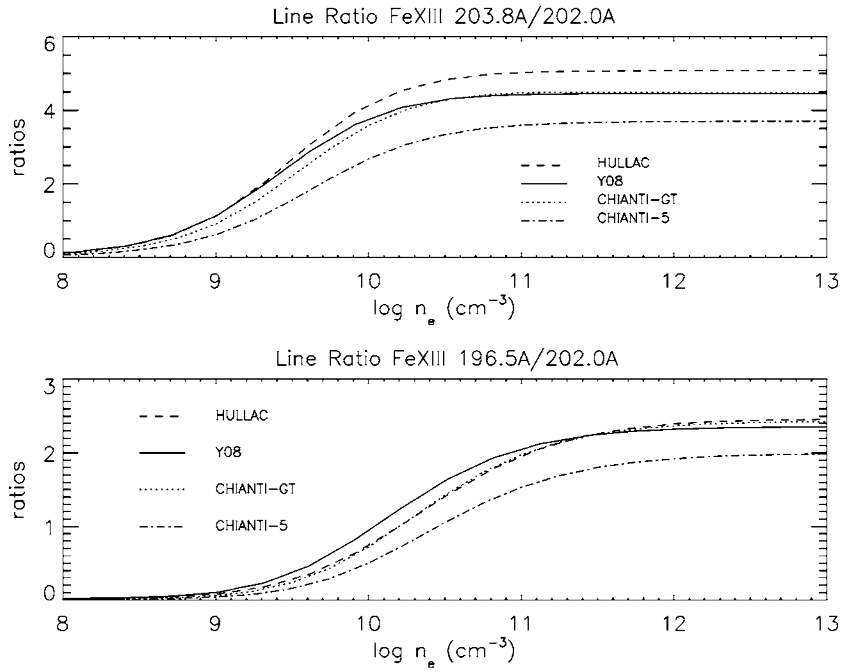

Figure 4. Theoretical intensity ratios of Fe XIII λ203.8/λ202.0 Å and λ196.5/λ202.0 Å. Dashed line for HULLAC; solid line calculated by Yamamoto et al. (2008) with the data of Aggarwal & Keenan (2005); dotted line for revised CHIANTI, and dash-dot line for CHIANTI v5.2.

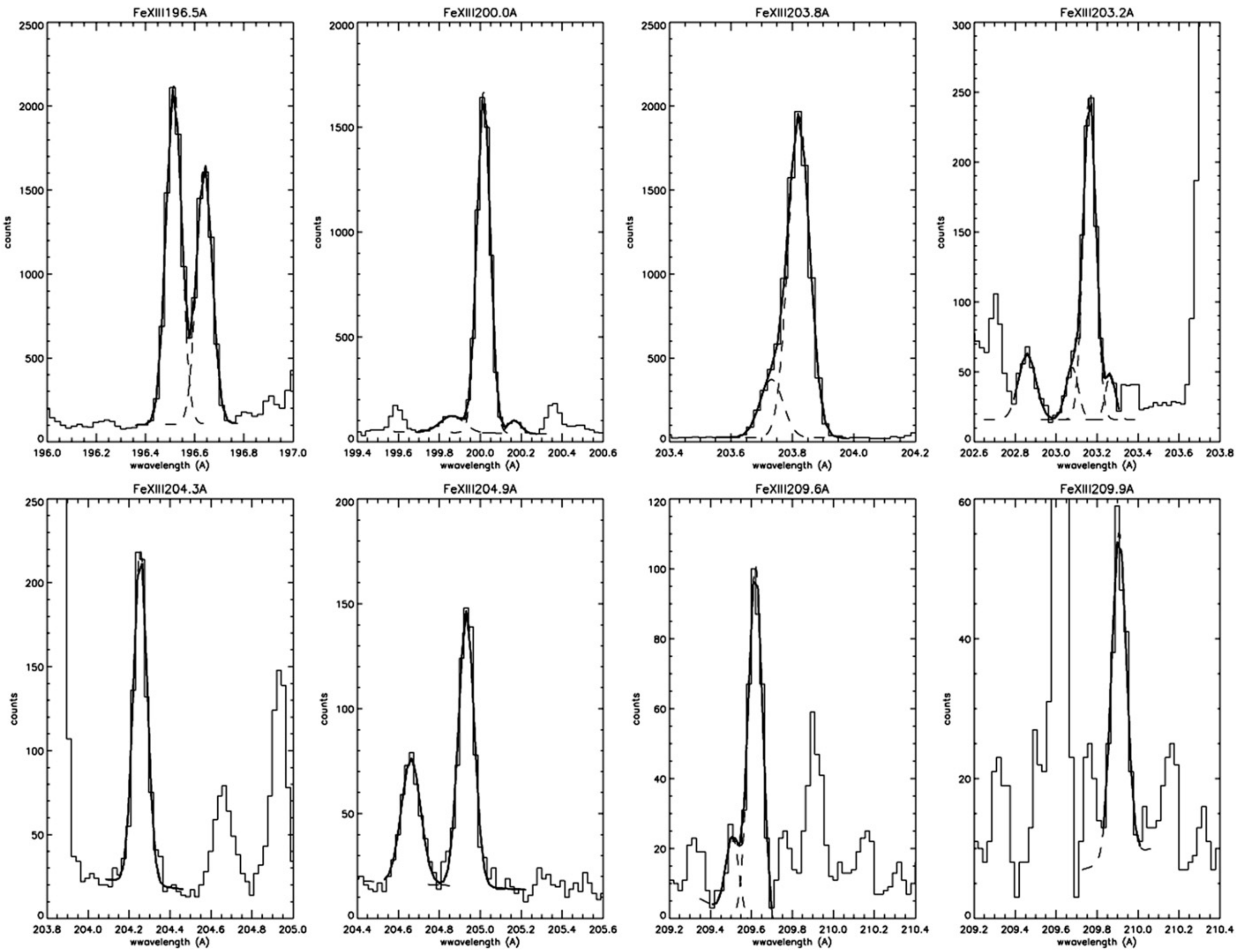

Figure 5. Examples of Gaussian multiple line fitting for the Fe XIII lines of λλ196.5, 200.0, 203.8, 203.2, 204.3, 204.9, 209.7, and 209.9 Å at the position of pixel number 281.

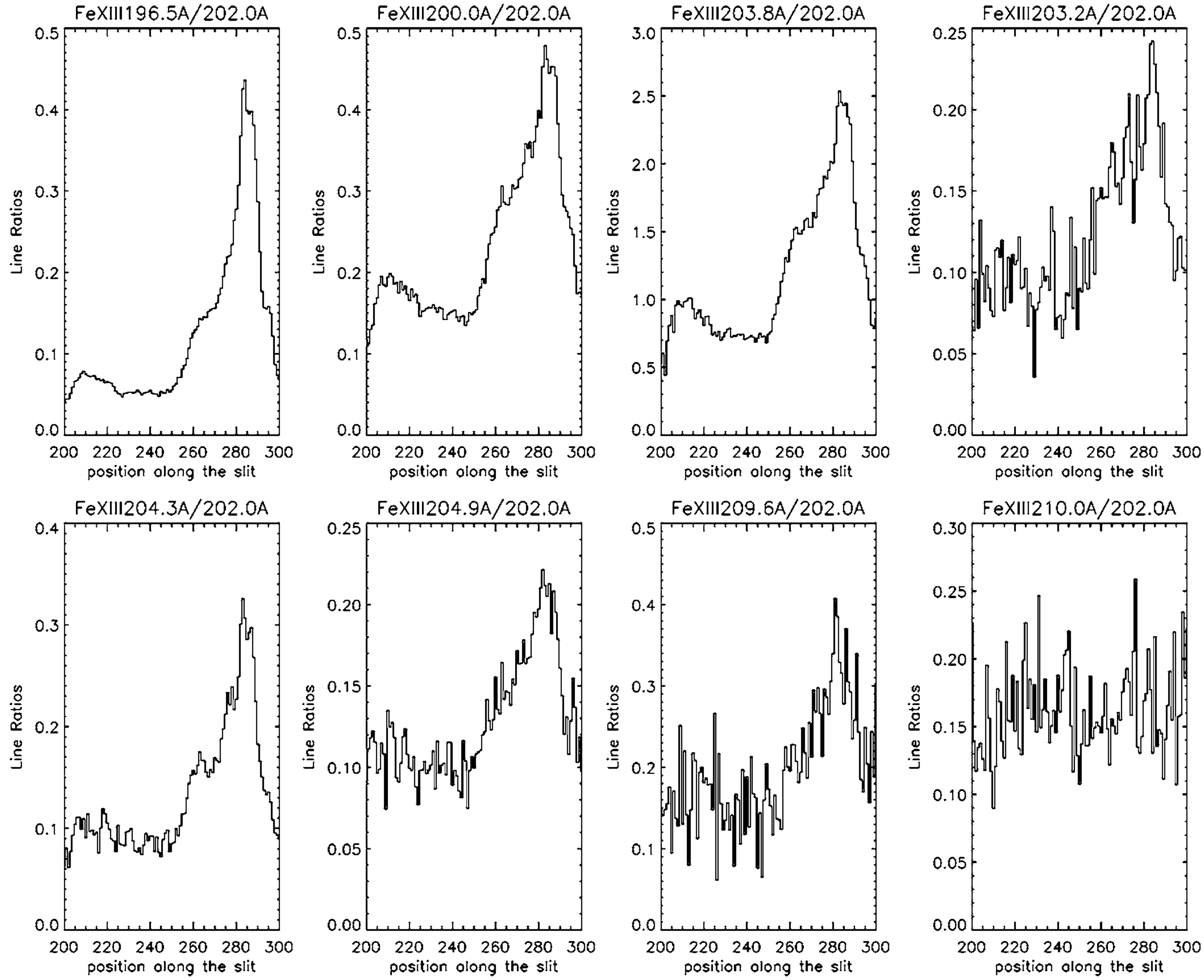

Figure 6. Intensity ratios of Fe xiii lines at the positions (pixel numbers: 200–300) along the slit.

can be estimated by fluctuations of the line ratios along the slit. For the ratios involving the strongest lines (λ196.5/λ202.0, λ200.0/λ202.0, and λ203.8/λ202.0), the relative errors of the intensity ratios are as small as 0.01, while for the weaker lines, the amplitudes of fluctuation can exceed 0.1. All ratios except λ209.9/λ202.0 show similar features in the ratio plots, reflecting a consistent response to plasma density variation along the EIS slit. This confirms that the ratios are behaving as expected from the theoretical predictions (Figure 3). The λ209.9/λ202.0 ratio is predicted to be insensitive to the plasma density and this is clearly seen in the bottom right panel of Figure 6. Averaging the measured line ratio over a 101 pixel region along the slit (see the top left panel of Figure7) gives a value of 0.162 $\pm$ 0.033. This value is closer to the value of 0.150 from the CHIANTI-GT model, rather than the value of 0.204 from the Y08 model. However, as the λ209.9 line is located at the long wavelength edge of the EIS wavelength band, the uncertainties in sensitivity of the EIS instrument must be considered. In our analysis, the calibration performed at Naval Research Laboratory (NRL) before the launch is adopted to obtain the spectral sensitivity of the EIS instrument (Korendyke et al. 2006).

Considering the seven ratios in Figure 6 that are sensitive to density, we use the Y08 and CHIANTI-GT models to convert the measured line ratios to density, and these are plotted in Figure 7. The top left panel shows the total intensity variation of the Fe xiii λ202.0 line along the slit. Here the intensity is derived from the fitting, namely by multiplying the peak intensity and the line width. The interval between the dotted lines (pixel numbers 200–300) is the region chosen for deriving the density structure of the active region shown in the remaining seven panels of Figure 7. Note that the pixel size along the slit corresponds to 1″ in the spatial direction (Culhane et al. 2007).

The two line ratios recommended by Keenan et al. (2007)—λ200.0/λ202.0 and λ203.2/λ202.0)—and the two recommended by Young et al. (2007)—λ196.5/λ202.0 and λ203.8/λ202.0—are found to yield very similar densities from both the Y08 and CHIANTI-GT models, particularly so from the Y08 model. Note that the maximum density in the AR10921 data set is around $10^{9.5}$ cm^{-3} so it is not possible to test the high density limits of the ratios, where a number of significant differences are seen in Figure 3.

For the λ196.5/λ202.0 ratio the CHIANTI-GT model yields systematically higher densities by 0.1–0.2 dex, as the theoretical ratio curve lies below the Y08 curve over the density range 10^8–$10^{11.5}$ cm^{-3}. The Y08 densities are more consistent with the other ratios. Although the recommended λ203.2/λ202.0 ratio

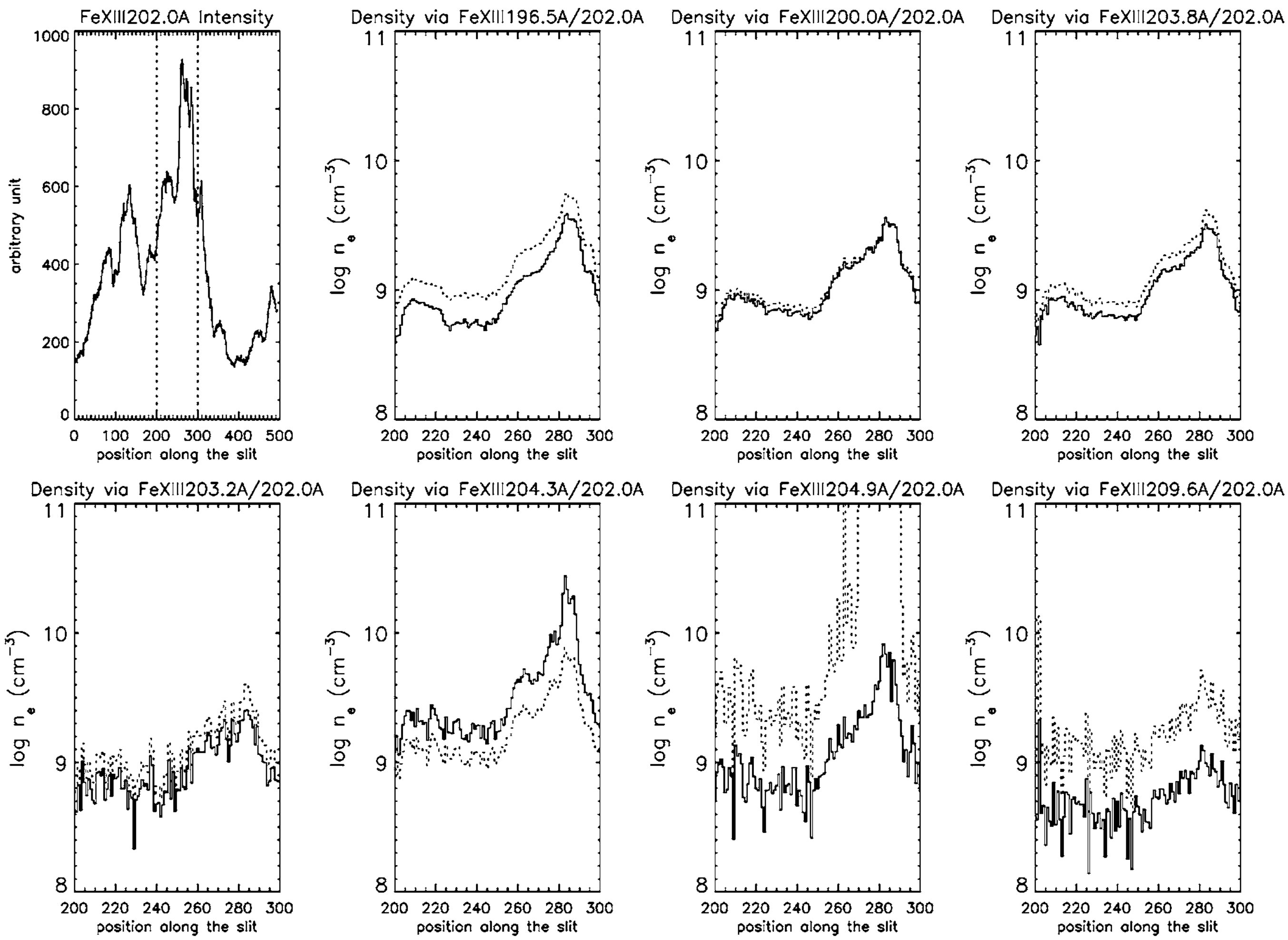

Figure 7. Densities derived from observed line ratios at the positions (pixel numbers: 200–300) along the slit. Total intensity of Fe XIII λ202.0 is plotted in the top-left panel. Solid lines are for the model of Y08 and dotted lines are for CHIANTI-GT.

gives consistent densities, we note the derived densities are more noisy than for the other three recommended ratios as the λ203.2 line itself is rather weak (10%–25% of the λ202.0 line), and the large intensity difference between the two lines might increase errors due to poor signal-to-noise ratio (S/N).

The density values from the four recommended ratios are similar and consistent to those derived from the density-sensitive line pairs of the Fe XI, Fe XII, Fe XIV ionization stages (Watanabe et al. 2007), although the analysis was rather preliminary and done by single Gaussian fitting. It is also interesting to note that in Figure 7 the intensity maximum of Fe XIII λ202.0 does not exactly correspond to the density maximum, but rather corresponds to the active region core, where the higher temperature lines, possibly originating from Ca XV, Ca XVI, and Fe XVII ions, are observed (Watanabe et al. 2007). The density of this high-temperature region could be increased by a micro-flare like activity.

For the remaining three ratios shown in Figure 7 the differences between the two models are more significant. If we assume the best of the recommended ratios is λ200.0/λ202.0 (due to the almost perfect agreement between the Y08 and CHIANTI-GT models), then the CHIANTI-GT model gives better agreement for λ204.3/λ202.0 and λ204.9/λ202.0, but the Y08 model gives better agreement for λ204.9/λ202.0.

These problems can be investigated further by studying the line ratios that are weakly sensitive to the plasma density as identified by Keenan et al. (2007). Figure 8 plots measured ratio values against the densities derived from the λ200.0/λ202.0 diagnostic for six ratios, including the λ209.9/λ202.0 branching ratio discussed earlier. In each plot the predictions from the two theoretical models, as well as the Y08+GRASP13 model, are overplotted. For the two ratios λ200.0/λ203.8 and λ203.2/λ200.0, the theoretical predictions are in reasonable agreement and the measured ratio values are close to the theoretical values. This explains why the density ratios involving these emission lines are in good agreement (Figure 7).

For λ204.3/λ200.0 the observed ratios lie above both the CHIANTI-GT and Y08 predictions, although the CHIANTI-GT values are in better agreement, and the Y08+GRASP13 results approach to the CHIANTI-GT locus. This helps explain why the density diagnostic by CHIANTI-GT for λ204.3/λ202.0 is in better agreement with the recommended diagnostics than the Y08 ratio. Similarly for the λ209.6/λ204.3 weakly sensitive ratio in Figure 8, the CHIANTI-GT model gives better agreement with the observations than the Y08 model, which then helps explain why the CHIANTI-GT model yields more consistent densities for the λ209.6/λ202.0 density diagnostic.

For the λ204.9/λ200.0 weakly sensitive ratio the measured ratio values are in close agreement with the predictions from the Y08 model (Figure 8), but the CHIANTI-GT predictions are well below the measured values. This suggests that the CHIANTI-GT model for the λ204.9 line is not correct,

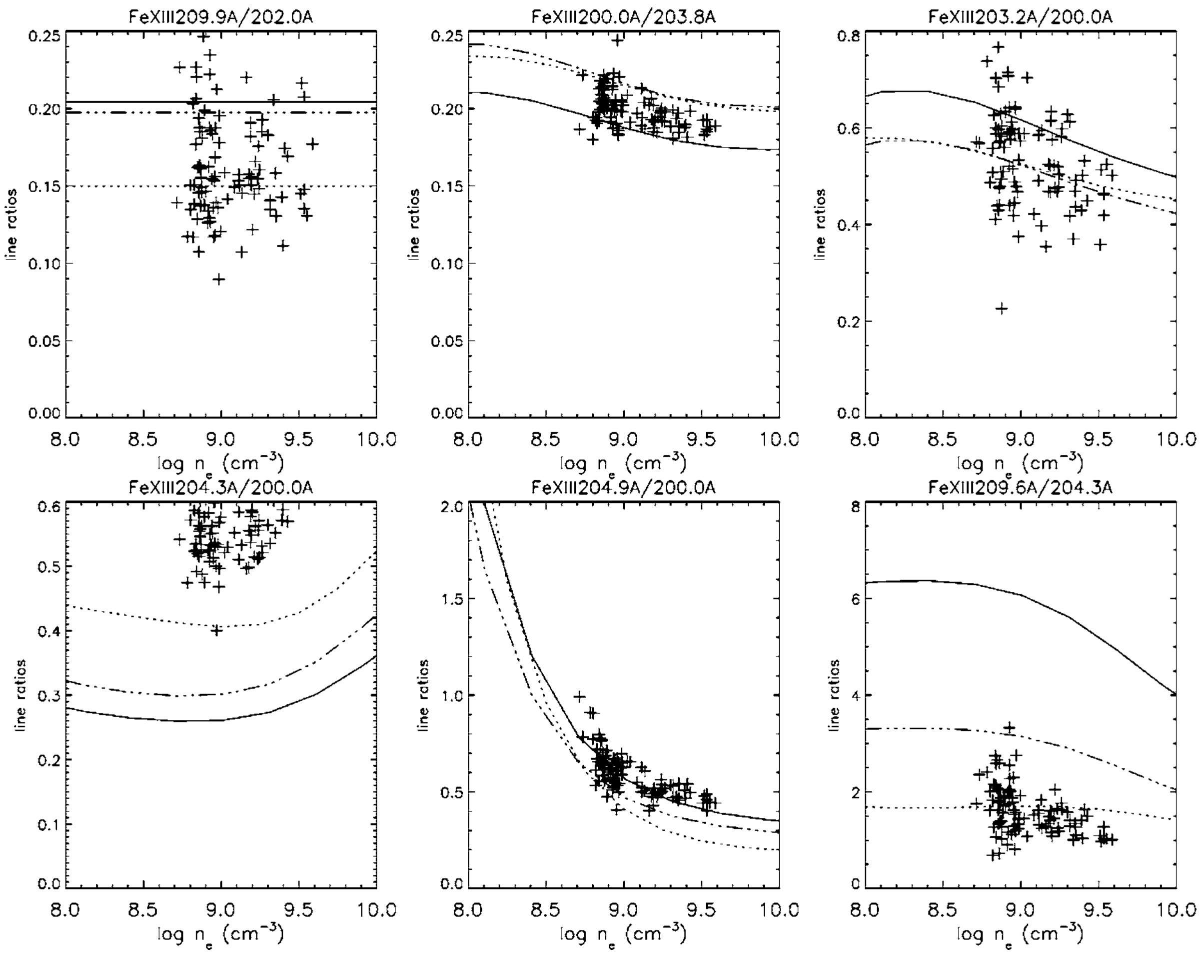

Figure 8. Weakly n_e dependent line ratios: solid curves are theoretical predictions by Aggarwal & Keenan (2005) calculated by the Y08 model (see the text), dotted curves those by the CHIANTI-GT model. Observed densities are determined by the Fe xiii λ200.0/λ202.0 Å line ratio. Solid lines are for the model of Y08, dotted lines for CHIANTI-GT, and dash-three-dots lines are for the model of Y08 configuration with GRASP13 radiative transition probabilities (Y08+GRASP13).

helping to explain why the CHIANTI-GT densities from the λ204.9/λ202.0 ratio are in poor agreement with the recommended density diagnostics (Figure 7). In this particular case, the adoption of the Y08+GRASP13 calculation does not improve, but degrades the degree of fitting to observation.

Taking the line ratio of λ209.6/λ209.9 located very close to the edge of the EIS longer waveband could eliminate the issue of EIS spectral calibration. Note that the line ratio of λ209.9 to λ202.0 is density insensitive. Figure 9 shows densities derived from this line intensity ratio. In Figure 9, the CHIANTI-GT predictions always give more-or-less consistent results to those derived from the recommended line pairs, while a large systematic difference somewhat reduces, but does not disappear, in the Y08 model, and almost disappear in the Y08+GRASP13 model, although the radiative transition probabilities remain different in both cases, as seen in Table 1. It is concluded that the CHIANTI code combined with the EIS spectral sensitivity calibration (Korendyke et al. 2006) provides consistent density information estimated by both the λ209.6/λ202.0 and λ209.6/λ209.9 line ratios.

In summary, the CHIANTI-GT and Y08 models predict densities from the four density diagnostics recommended by Keenan et al. (2007) and Young et al. (2007) that are in very good agreement. Of the two models, the Y08 model yields the best agreement. From comparisons of ratios that are weakly sensitive to density, there are found to be problems for the λ204.3, λ209.6, and λ209.9 lines predicted from the Y08 model, while the CHIANTI-GT model does not predict well the λ204.3 and λ204.9 lines.

5. FLARE DATA SET

The AR10921 data set discussed in the previous section provided tests of the Fe xiii density diagnostics for densities up to $10^{9.5}$ cm^{-3}. Tests for higher densities, particularly the high density limits of the ratios, require observations of flares. At the temperature of formation of Fe xiii, $\log T = 6.2$, the ion provides density information at the footpoints of flaring loops.

For a study of high density plasma we use the EIS observation of a C-class flare on 2007 January 16 discussed earlier. The CCD observing windows were set to observe only the λ202.0 and λ203.8 lines of Fe xiii, so only this density sensitive line ratio can be studied. The emission lines were fitted with Gaussians as for the AR10921 data set, and Figure 10 shows the values of the λ203.8/λ202.0 ratio, plotted against the intensity of the λ202.0 line, at every pixel in the 240×240 pixel image from the EIS raster. For comparison, the ratio values from the AR10921 data set discussed in the previous section are also plotted. The ratio values are mostly higher in the flare data set, implying higher densities. The horizontal dotted line in Figure 10 shows the high density limit of the λ203.8/λ202.0 ratio predicted from the Y08 model. By comparison with the theoretical ratio plot from Figure 3 we see that the highest ratio values correspond to densities $\geqslant 10^{11}$ cm^{-3}. Averaging the ratio values where the

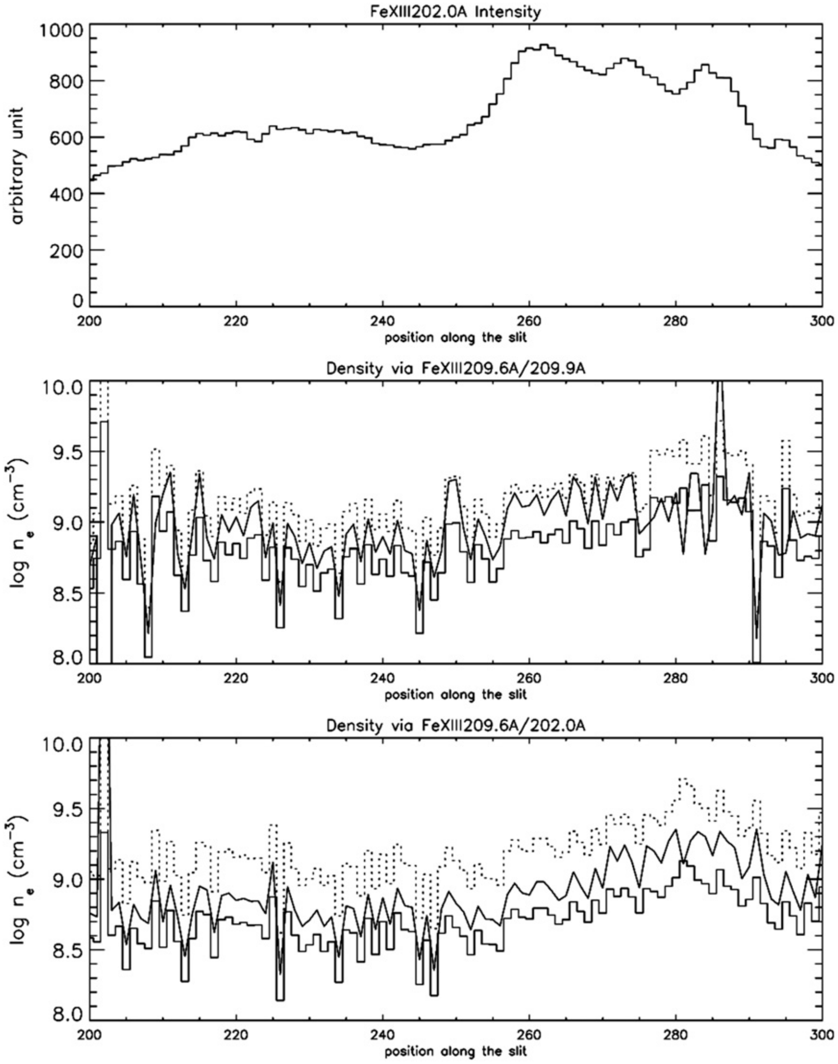

Figure 9. Densities derived from 209.6/202.0 Å and 209.6/209.9 Å intensity ratios at the positions (pixel numbers: 200–300) along the slit. Total intensity of Fe XIII λ202.0 is plotted in the top-left panel. Solid lines are for the model of Y08, dotted lines for CHIANTI-GT, and solid splines are for the model of Y08+GRASP13 (see the text).

intensity of the λ202.0 line is ⩾ 40 (arbitrary units) we find an average observed value of 4.34, which we take to be the measured high density limit of λ203.8/λ202.0.

Recently Yamamoto et al. (2008) made a TESPEL (tracer-encapsulated solid pellets) experiment in the Large Helical Device (LHD) at the National Institute for Fusion Science (NIFS), and found that the value of the line ratio at the high density limit was somewhat below 4. They attributed the discrepancy between the laboratory measurement and solar observation to the oxygen lines possibly blended with Fe XIII λ202.0.

To investigate this further, the spatial region where the Fe XIII λ203.8/λ202.0 ratio is ⩾ 3.7 is indicated in Figure 11, where monochromatic images from Fe XIII λ202.0, Fe XIII λ203.8, Fe XVII λ254.8, and Fe XXIII λ263.8 are also shown. The best correlation is achieved with the intensity maps of the Fe XIII lines themselves. If the reason for the higher high density limit found from the EIS measurements compared with the laboratory measurements is due to an unidentified blending line at 203.8 Å in the solar spectrum, then our observation that high ratio values are correlated with the Fe XIII intensity images implies that the blending line must be formed at temperatures close to Fe XIII; thus a transition region temperature blending line can be ruled out. However, the possibility of a blending line at Fe XIII temperatures was ruled out in the laboratory experiment (Yamamoto et al. 2008). We thus believe that the λ203.8 line is unblended and that the solar measurements are in agreement with the Y08 theoretical model.

6. SUMMARY

The diagnostic capability of Fe XIII line features seen in the EIS observing wavelengths has been investigated. Full CCD slit spectra of the EIS first light active region AR10921 observed in the short wavelength band (170–210 Å) are used to provide a data set of Fe XIII emission lines, and their intensities are compared with two theoretical models for density diagnostics: the first is a modification of the CHIANTI v5.2 model that uses the Gupta & Tayal (1998) electron collision file, and the second is the model of Yamamoto et al. (2008) that uses the electron collision data of Aggarwal & Keenan (2005). In the density range from $10^{8.5}$ to $10^{9.5}$ cm,$^{-3}$ the four density diagnostics recommended by Keenan et al. (2007) and Young et al. (2007) all give consistent densities. These

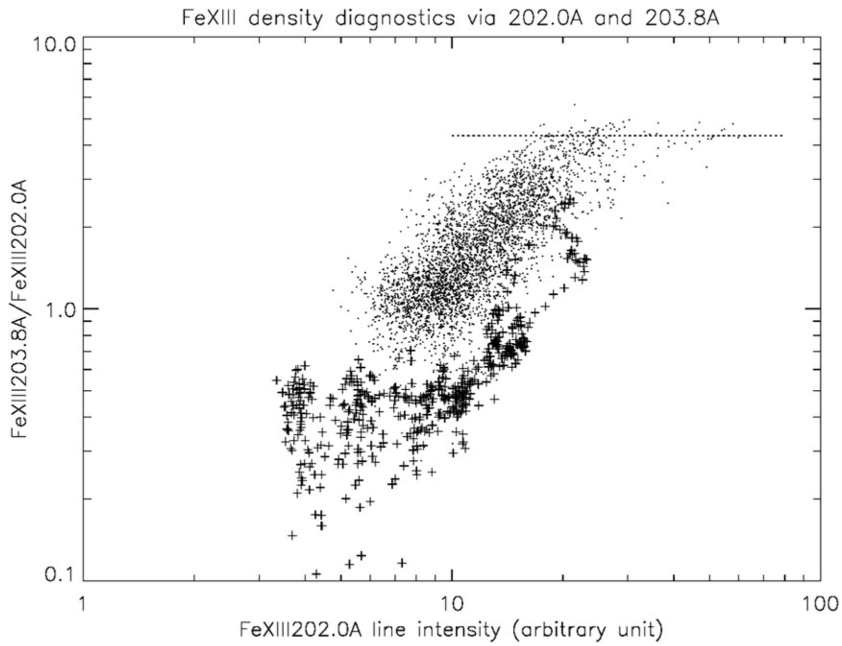

Figure 10. Fe XIII λ203.8/λ202.0 Å line ratios (dots) in a small flare (2007 January 16). Plus marks indicate the data points of AR10921 (2006 November 6) in the same arbitrary unit of intensity. Dotted horizontal line shows the average value of 4.34 obtained from the data points exceeding 40 in the intensity unit.

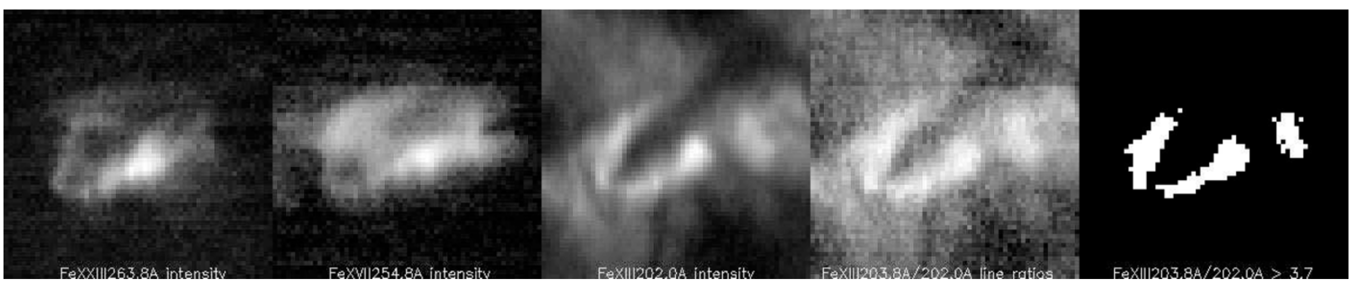

Figure 11. Monochromatic images of Fe XXIII, Fe XVII, and Fe XIII lines, line ratio of Fe XIII λ203.8/λ202.0 Å, and the same panel showing the area of the ratio above 3.7.

ratios are λ196.5/λ202.0, λ200.0/λ202.0, λ203.2/λ202.0, and λ203.8/λ202.0. These are all strong lines appearing in the EIS waveband except λ203.2. The Yamamoto et al. (2008) model gives slightly better consistency between the ratios than the modified CHIANTI model for these strong line pairs. For other Fe XIII lines we find problems with both of the theoretical models: from the Yamamoto et al. (2008) model, λ204.3 and λ209.6 are not well predicted, while for the modified CHIANTI model λ204.3 and λ204.9 are inconsistent with observations. They are generally weak lines seen in the EIS waveband, and the problems with the λ209.6 and λ209.9 may be partly due to the instrument calibration as they lie very close to end of the EIS waveband.

The accuracy of the high density limit of the important λ203.8/λ202.0 density sensitive ratio has also been studied using an EIS observation of a C-class flare from 2007 January 16. We find the measured ratio is consistent with the theoretical predictions from both the Yamamoto et al. (2008) and modified CHIANTI models.

Hinode is a Japanese mission developed and launched by ISAS/JAXA, collaborating with NAOJ as domestic partner, NASA and STFC (UK) as international partners. Scientific operation of the *Hinode* mission is conducted by the *Hinode* science team organized at ISAS/JAXA. This team mainly consists of scientists from institutes in the partner countries. Support for the postlaunch operation is provided by JAXA and NAOJ (Japan), STFC (UK), NASA (USA), ESA, and NSC (Norway). This work is partly carried out at the NAOJ *Hinode* Science Center, which is supported by the Grant-in-Aid for Creative Scientific Research: "The Basic Study of Space Weather Prediction" from MEXT, Japan (Head Investigator: K. Shibata), generous donations from Sun Microsystems, and NAOJ/NINS internal funding. It is also supported by NINS inter-institute collaborative program for Creation of New Research Area (Head Investigator: T. Watanabe), and by NIFS/NINS under the project of Formation of International Network for Scientific Collaborations (Head Investigator: H. Yamada).

REFERENCES

Aggarwal, K. M., & Keenan, F. P. 2004, A&A, 418, 371
Aggarwal, K. M., & Keenan, F. P. 2005, A&A, 429, 1117
Bar-Shalom, A., Klapisch, M., & Oreg, J. 2001, J. Quantum Spectrosc. Radiat. Transfer, 71, 179
Brosius, J. W., Davila, J. M., & Thomas, R. J. 1998, ApJS, 119, 255
Brosius, J. W., Davila, J. M., Thomas, R. J., & Monsignori Fossi, B. C. 1996, ApJS , 106, 143
Brosius, J. W., Davila, J. M., Thomas, R. J., & Landi, E. 2000, ApJ, 543, 1016
Brown, C. M., Feldman, U., Seely, J. F., & Korendyke, C. M. 2008, ApJS, 176, 511
Culhane, J. L., et al. 2007, Sol. Phys., 243, 19

Dere, K. P., Landi, E., Mason, H. E., Mosignori-Fossi, B. F., & Young, P. R. 1997, A&AS, 125, 149
Dere, K. P., Landi, E., Young, P. R., & Del Zanna, G. 2001, ApJS, 134, 331
Faucher, P., & Landman, D. A. 1977, A&A, 54, 159
Fawcett, B. C., & Mason, H. E. 1989, ADNDT, 43, 245
Gupta, G. P., & Tayal, S. S. 1998, ApJ, 506, 464
Jupén, C., Isler, R. C., & Träbert, 1993, MNRAS, 264, 627
Keenan, F. P., Jess, D. B., Aggarwal, K. M., Brosius, J. W., & Davila, J. M. 2007, MNRAS, 376, 205
Korendyke, C. M., et al. 2006, Appl. Opt., 45, 8674
Landi, E. 2002, A&A, 382, 1106
Landi, E., et al. 2006, ApJS, 162, 261
Landman, D. A. 1975, A&A, 43, 285
Matsuzaki, K., et al. 2007, Sol. Phys. , 243, 87
Penn, M. J., & Kuhn, J. R. 1994, ApJ, 434, 807
Skobelev, I., Murakami, I., & Kato, T. 2006, NIFS-DATA-95, 1
Skobelev, I., Murakami, I., & Kato, T. 2007, NIFS-DATA-99, 1
Watanabe, T., et al. 2007, PASJ, 59, S669
Yamamoto, N., et al. 2008, ApJ, 689, 646
Young, P. R. 2004, A&A, 417, 785
Young, P. R., et al. 2007, PASJ, 59, S857
Young, P. R., Watanabe, T., Hara, H., & Mariska, J. T. 2009, A&A, in press